Geophysical Research Letters

Diurnal Variation of Liquid Water Path Derived From Two Polar-Orbiting FengYun-3 MicroWave Radiation Imagers

Fei Tang[1,2] (iD) and Xiaolei Zou[3] (iD)

[1]Chinese Academy of Meteorological Sciences, China and State Key Laboratory of Severe Weather, Beijing, China, [2]Nanjing University of Information Science and Technology (NUIST), Joint Center of Data Assimilation for Research and Application, College of Atmospheric Science, Nanjing, China, [3]University of Maryland, Earth System Science Interdisciplinary Center (ESSIC), College Park, MD, USA

Abstract MicroWave Radiation Imagers (MWRIs) onboard the afternoon FengYun-3 (FY-3B) and midmorning FengYun-3C (FY-3C) satellites provide global observations almost 4 times a day at any location. This study examines the diurnal cycle of the liquid water path (LWP) over the southeast Pacific Ocean using MWRI data. A double-difference calibration method is first used to evaluate the MWRI calibration bias based on Tropical Rainfall Measuring Mission Microwave Imager (TMI) measurements. LWP diurnal cycle characteristics are derived from FY-3B/C MWRI data measured in 2014. The diurnal variation of LWP from combined FY-3B/C MWRI measurements are consistent with that derived from Tropical Rainfall Measuring Mission Microwave Imager data. Maximum and minimum LWPs occurred in the early morning and afternoon, respectively. The largest diurnal amplitude (~40% of the mean LWP) was located near 85°W/20°S. The diurnal amplitude varied from season to season. MWRI data can provide important constraints for models simulating the cloud diurnal cycle.

Plain Language Summary MicroWave Radiation Imager (MWRI) dual-polarization measurements at 10.65, 18.7, 23.8, 36.5, and 89 GHz can be combined to retrieve the liquid water path (LWP) in the atmosphere over ocean surfaces. The Chinese FengYun-3B and FengYun-3C satellites provide MWRI observations during their midmorning and afternoon orbits, respectively, allowing the diurnal variations of LWP to be observed globally by such polar-orbiting satellites. The diurnal variations of LWP are important for understanding hydrometeorological processes in the atmosphere and for validating LWP numerical weather prediction models. It is shown that in 2014, FengYun-3B and FengYun-3C MWRI-derived LWP retrievals compared well with those derived from the Tropical Rainfall Measuring Mission Microwave Imager over the southeast Pacific Ocean. The intensity of the diurnal cycle varied from season to season and the largest diurnal amplitude (~40% of the mean LWP) was located near 85°W/20°S.

1. Introduction

Cloud radiative properties and their changes over time are a major contributor to the global climate. Cloud radiative properties depend on the hydrometeor type (Shupe & Intrieri, 2004; Taylor & Ghan, 1992). The cloud liquid water path (LWP) is one type of hydrometeor type, and their geographic distribution and variation over space and time affect the climate. With the development of numerical weather forecast and climate models, LWP can be simulated using a dynamic framework and cumulus parameterization schemes in numerical models. However, these models cannot perfectly simulate changes in real atmospheric physical parameters. Therefore, a better understanding of LWP diurnal variations will be helpful in validating LWP results from numerical models.

Satellite microwave imager observations have been widely used to retrieve LWP from around the globe. These include observations from the Special Sensor Microwave Imager onboard the Defense Meteorological Satellite Program series of satellites (Weng & Grody, 1994), the Tropical Rainfall Measuring Mission (TRMM) Microwave Imager (TMI) and its successor, the Global Precipitation Measurement (GPM) microwave imager (Duncan & Kummerow, 2016; Kummerow et al., 2001), and the Advanced Microwave Scanning Radiometer EOS (AMSR-E) carried by the Aqua satellite and its successor, the AMSR2 onboard the Global Change Observation Mission-Water 1 satellite (Kachi et al., 2008). The Defense Meteorological Satellite Program satellite series have both early morning and midmorning orbits. The TRMM and GPM satellites have nonsun-synchronous orbits and provide sampling of the entire diurnal cycle over several months of

Table 1
MWRI and TMI Channel Characteristics

MWRI					
Frequency (GHz)	Polarization	IFOV (km × km)	Bandwidth (MHz)	Samples/scan	NEΔT (K)
10.65	V/H	51 × 85	180	254	0.41
18.7	V/H	30 × 50	200	254	0.27
23.8	V/H	27 × 45	400	254	0.33
36.5	V/H	18 × 30	400	254	0.40
89	V/H	9 × 15	3000	254	0.31
TMI (postboost)					
10.65	V/H	73 × 43	100	104	0.6
19.35	V/H	35 × 21	500	104	0.7
21.3	V	26 × 21	200	104	0.9
37	V/H	18 × 10	2000	104	0.4
85.5	V/H	8 × 6	3000	208	0.7

Note. IFOV: instantaneous field-of-view; MWRI: MicroWave Radiation Imager; NEΔT: temperature sensitivity; TMI: Tropical Rainfall Measuring Mission Microwave Imager; V/H: vertical/horizontal.

orbits. However, TRMM is restricted to tropical regions and GPM only to 68° of latitude. Both AMSR-E and AMSR2 are in afternoon polar orbits. China launched the afternoon FengYun-3B (FY-3B) and midmorning FengYun-3C (FY-3C) satellites on 5 December 2010 and 23 September 2013, respectively, to provide global MicroWave Radiation Imager (MWRI) observations almost 4 times a day at any location. The MWRIs onboard both satellites observe critical environmental parameters such as ocean wind speed, sea surface temperature, and precipitation. The MWRI 10.65-GHz channel can penetrate a cloudy/rainy atmosphere and is commonly used to retrieve LWPs >3 mm. The 36 and 89-GHz channels can be used to retrieve the LWP in low stratus clouds (LWP < 0.2 mm). Tang and Zou (2017) developed a combined MWRI multichannel algorithm to retrieve LWP in nonraining and raining clouds over oceans.

FengYun-3B/C MWRI observations from both midmorning and afternoon orbits are available for the first time. This study aims at estimating LWP diurnal variations over the southeast Pacific Ocean (115°W–75°W, 40°S–0) using combined FY-3B/C MWRI data. The diurnal cycle of the low-level stratiform cloud deck is a significant mode of variability in the southeast Pacific Ocean (Garreaud & Munoz, 2004; Minnis & Harrison, 1984; O'Dell et al., 2008). In an early study, Zuidema and Hartmann (1995) estimated the LWP diurnal variability based on observations from the morning and afternoon overpasses of the Special Sensor Microwave Imager satellites over the southeast Pacific region. This region is selected because (1) moderate to heavy precipitation is infrequent here so the uncertainty in LWP is relatively small, (2) there are little to no frozen particles in the low-altitude stratiform cloud fields here, and (3) deep convection, midlatitude frontal disturbances, and widespread cirrus are infrequent (O'Dell et al., 2008). The semidiurnal cycle, which could be important off the west coast of South America (O'Dell et al., 2008), cannot be resolved by FY-3B/C MWRI measurements so is not considered in this study. MWRI channels are first cross-calibrated, then used for LWP retrievals. These retrievals are finally compared with TRMM TMI LWP retrievals.

2. Data and Methods

2.1. MWRI and TMI Data

The MWRIs onboard both FY satellites measure radiances at 10.65, 18.7, 23.8, 36.5, and 89 GHz. Each frequency corresponds to two channels with dual polarizations. The TMI has a total of nine channels: 10.65, 19.35, 37, and 85.5 GHz with dual polarizations (vertical and horizontal) and a 21.3-GHz channel with vertical polarization only. MWRI and TMI instrument characteristics are given in Table 1, and more details can be found in Tang and Zou (2017) and Kummerow et al. (1998), respectively.

MicroWave Radiation Imager Level-1 brightness temperature (T_b) data from the National Satellite Meteorological Center of the China Meteorological Administration (http://satellite.nsmc.org.cn/PortalSite/ Data/Satellite.aspx) are used. TMI-derived T_bs from version 7 of the Level 1B calibrated radiances product are also used (https://disc.gsfc.nasa.gov/datasets/TRMM_1B11_V7/summary?%20keywords%C2%A0=%C2%
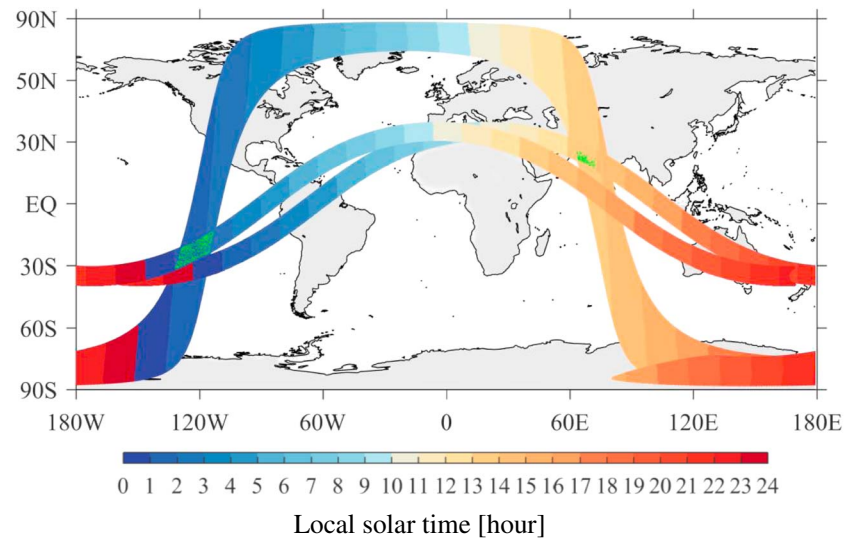
Figure 1. Local time distributions of one orbit of the FengYun-3B satellite carrying the MicroWave Radiation Imager (MWRI) and two consecutive orbits of the Tropical Rainfall Measuring Mission (TRMM) satellite carrying the TRMM Microwave Imager (TMI) on 1 January 2014. The green points show collocated observations identified by the following criteria: 10-min maximum time differences and 1-km maximum distances between MWRI and TMI observations.

A01B11) and include the implementation of a time-varying solar bias correction (Biswas et al., 2010; Gopalan et al., 2009). The study period is 1 January to 31 December 2014.

2.2. Cross-Calibration of FY-3B/C MWRI With TMI

A double-difference method is used to cross-calibrate FY-3B/C MWRI T_bs based on TMI radiances. Six months of FY-3B/C MWRI data from January to June 2014 are collocated with TMI observations using the following collocation criteria: a 10-min maximum time difference and a 1-km maximum distance between MWRI and TMI observations. Figure 1 shows local overpass times along the FY-3B MWRI and TRMM TMI orbits on 1 January 2014. Regions with collocated observations on this day are shown in green. Clear-sky data over oceans are defined as those data with LWP $< 10^{-4}$ mm (Tang & Zou, 2017).

The Community Radiative Transfer Model developed by the U.S. Joint Center for Satellite Data Assimilation (Han et al., 2007; Weng, 2007) is used to simulate T_b for all selected MWRI observations. Model inputs include sensor information such as zenith angles and locations, and model forecasts for surface parameters and temperature and humidity profiles. The National Centers for Environmental Prediction Global Data Assimilation System is used for the model simulations.

For brevity, MWRI and TMI observations are denoted as O, and Community Radiative Transfer Model simulations are denoted as B. The double difference (DD) is expressed as

$$DD_{MWRI/TMI} = (O_{MWRI} - B_{MWRI}) - (O_{TMI} - B_{TMI}). \qquad (1)$$

From equation (1), model errors can cancel out, and the effect of incident-angle differences between the MWRI and the TMI is eliminated (Yang et al., 2011).

Figure 2 shows FY-3B/C 89-GHz MWRI and 85.5-GHz TMI mean DDs and their standard deviations at 1° latitude intervals. DD varies with latitude and is generally <1.5 K with standard deviations within 2.5 K. DDs for other channels have similar characteristics (figures omitted). The figure also suggests that biases among FY-3B/C MWRI ascending and descending orbit measurements must first be eliminated before retrieving LWP to ensure coherent deviations when calculating LWP diurnal cycles.

2.3. Method Used to Calculate LWP Diurnal Cycles

After cross-calibration, the multichannel retrieval algorithm developed by Tang and Zou (2017) is used to derive LWP. Data from FY-3B/C MWRI channels 10.65, 18.7, and 23.8 GHz and 36.5-GHz vertical and 89-GHz
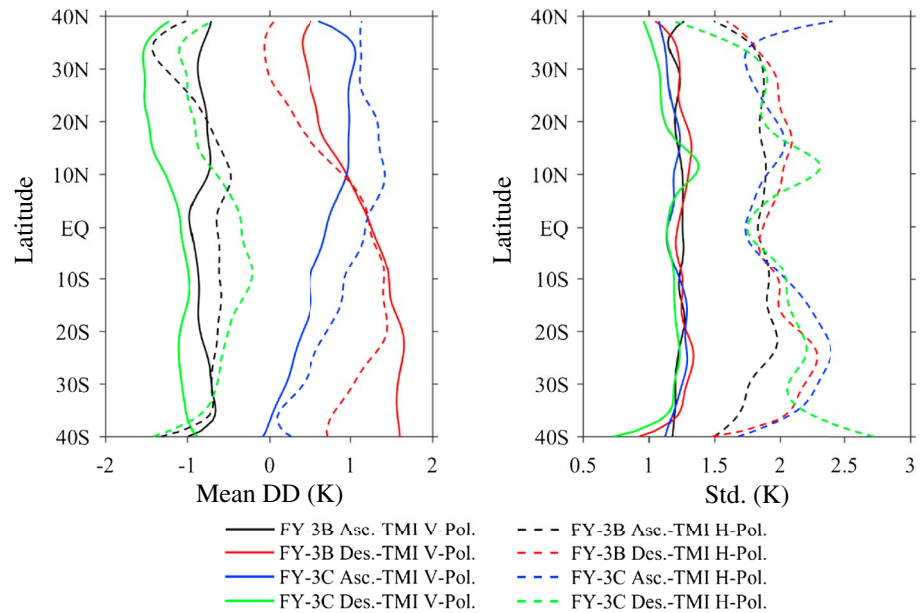
Figure 2. FengYun-3B/C 89-GHz MicroWave Radiation Imager and 85.5-GHz Tropical Rainfall Measuring Mission Microwave Imager (left) mean double differences (DDs) and (right) their standard deviations at 1° latitude intervals. DDs involving vertical and horizontal polarizations are shown as solid and dashed lines, respectively. Data are from January to June 2014.

horizontal polarizations are also used. When variations in T_b mainly depend on water vapor and LWP, measurements from two channels are sufficient for retrieving LWP (Grody & Ferraro, 1992; Hargens, 1992):

$$\text{LWP} = a_0[\ln(290 - T_{b1}) - a_1 - a_2 \ln(290 - T_{b2})], \tag{2}$$

where T_{b1} is the T_b of a channel that is sensitive to LWP and T_{b2} is the T_b located on the water vapor absorption line. The coefficients a_0, a_1, and a_2 are dependent on the T_bs of different channels, and their values are obtained through the statistical regression of observed T_bs. Given that TMI channels have similar frequencies and field-of-view sizes, equation (2) was also applied to these data as a reference. The coefficients a_0, a_1, and a_2 used in this study are given in Table 2.

Due to differences in the center frequencies and incident angles of the MWRI and TMI instruments, their T_bs for the same Earth scene are not the same. Therefore, the two sensors' coefficients a_1, a_2 are different. Tang and Zou (2017) give a detailed discussion about LWP retrieval errors and show that the algorithm can generate reasonable retrievals under rainy and nonrainy conditions over oceans.

Table 2
Equation (2) Coefficients a_0, a_1, and a_2 for MWRI and TMI Retrievals

TMI			
LWP_{chan}	a_0	a_1	a_2
10.65 V	−3.32	4.37	0.097
19.35 V	−2.44	2.47	0.48
37 V	−0.98	2.58	0.41
85.5H	−0.37	−2.50	1.56
MWRI			
10.65 V	−3.87	4.47	0.09
18.7 V	−1.94	3.03	0.37
36.5 V	−0.97	2.74	0.39
89H	−0.37	−3.08	1.68

Note. V: vertical; H: horizontal; MWRI: MicroWave Radiation Imager; TMI: Tropical Rainfall Measuring Mission Microwave Imager.

The diurnal cycle of LWP has a basic sinusoidal shape with a period of 24 hr at most locations (O'Dell et al., 2008). The FY-3B/C MWRI-retrieved LWPs are combined onto a 2.5° × 2.5° spatial grid for the following local standard times (LSTs): 0140, 1015, 1340, and 2215 LST. The diurnal cycle is estimated using the following sinusoidal equation (Chen et al., 2018):

$$\overline{\text{LWP}}_{\lambda,\varphi}(t) = A_0 + A_1 \cos(\omega t) + A_2 \sin(\omega t), \tag{3}$$

where $\overline{\text{LWP}}_{\lambda,\varphi}(t)$ is the estimated mean LWP at a particular latitude (φ), longitude (λ), and local time t (in hours) and $\omega = {2\pi}/{24}$ is the diurnal frequency. The coefficients A_0, A_1, A_2 are obtained by applying the least squares fitting method to the LWP time series sampled at the actual FY-3B/C satellite observation times. The amplitude and phase of the diurnal cycle are calculated as $A = \sqrt{A_1^2 + A_2^2}$ and $P = \arctan\frac{A_2}{A_1}$, respectively.
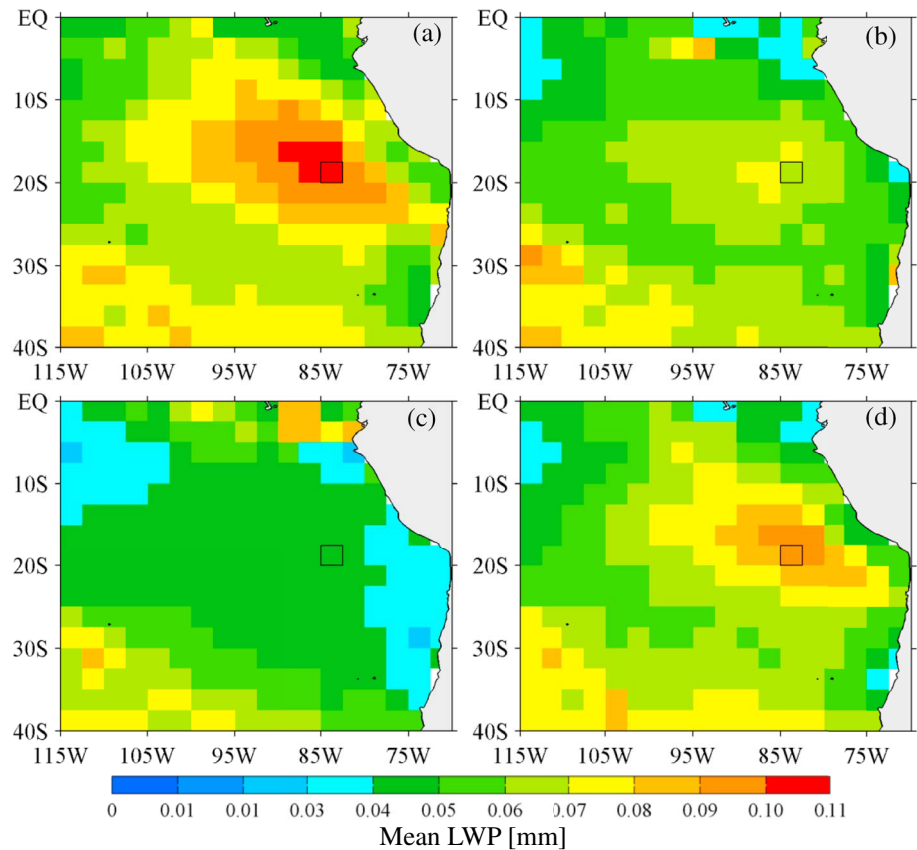
Figure 3. Annual mean liquid water path distributions in 2014 over the Southeast Pacific Ocean (115°W–70°W, 40°S–0) for (a) the FengYun-3B (FY-3B) descending orbit (0140 local equator crossing time, or ECT), (b) the FengYun-3C (FY-3C) descending orbit (1015 ECT), (c) the FY-3B ascending orbit (1340 ECT), and (d) the FY-3C ascending orbit (2215 ECT).

3. Results

3.1. Characterization of the LWP Diurnal Cycle

Figure 3 shows spatial distributions of the annual mean LWP over the study region (115°W–75°W, 40°S–0) derived from FY-3B/C MWRI data after cross-calibration between FY-3B/C MWRI and TMI data at 0140, 1015, 1340, and 2215 LST. The spatial resolution is 2.5° × 2.5°. MWRI-retrieved LWP values range from 0.01 to 0.11 mm over the southeast Pacific Ocean where low clouds dominate. A maximum in LWP (>0.1 mm) is seen at 0140 LST near 85°W/20°S (Figure 3a). A possible reason is that over the study region, deep convective clouds sometimes appear around that time (Gray & Jacobson, 1977). The smallest LWP values are seen around 1340 LST. These results are consistent with those from previous studies. The mean LWP decreased from 0.07 mm at 1015 LST (Figure 3b) to 0.05 mm at 1,340 mm (Figure 3c), after which it increased to 0.09 mm at 2215 LST (Figure 3d). Figure 3 also shows that LWP over most of the southeast Pacific Ocean area varies diurnally. The FY-3B/C satellites follow each other so greatly enhance the LWP temporal sampling rate.

That LWP displays strong variations around 85°W/20°S is already known. To further illustrate the LWP diurnal variations derived from FY-3B/C MWRI data, Figure 4 shows the diurnal cycle of LWP in the area outlined in black in Figure 3a, that is, 85°W–82.5°W, 20°S–17.5°S. The LWP diurnal cycle derived from TMI data is sinusoidal in shape with peaks and valleys at 0200 LST and 1400 LST, respectively. The amplitude of the diurnal cycle is ~0.03 mm. These results are consistent with Figure 1 in Wood et al. (2002). The LWP distributions derived from FY-3B/C MWRI data at their respective local times follow the TMI regression curve. We thus conclude that the diurnal cycle features of MWRI-derived LWP can be captured. Note that the calibration bias has an effect on the LWP diurnal cycle.
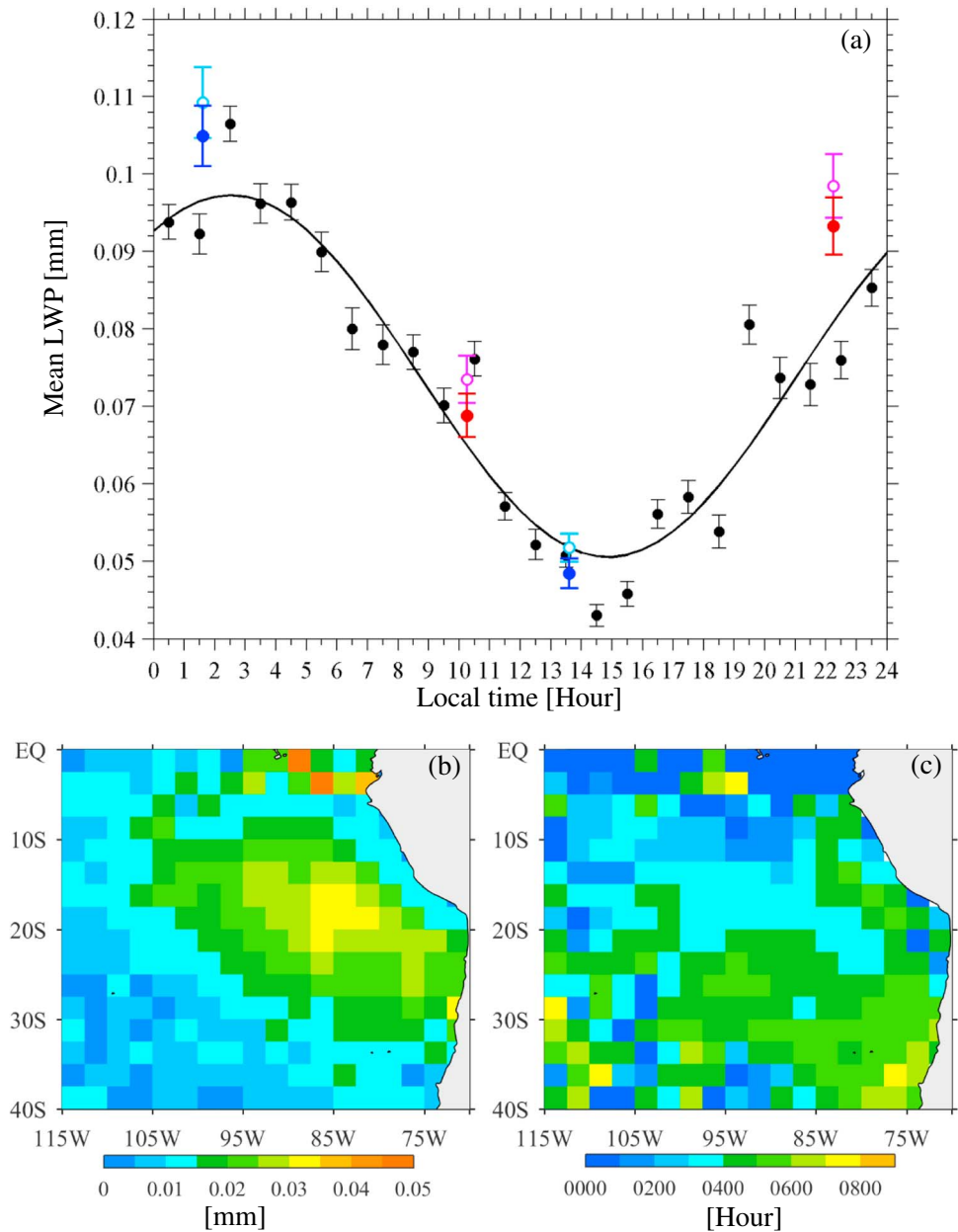
Figure 4. (a) The mean liquid water path (LWP) diurnal cycle in 2014 calculated from LWP retrieved from the Tropical Rainfall Measuring Mission Microwave Imager (TMI; black dots), the FengYun-3B MicroWave Radiation Imager (MWRI) before (cyan circles) and after (blue dots) cross-calibration, and the FengYun-3C MWRI before (magenta circles) and after (red dots) cross-calibration for the area outlined in black in Figure 3 (85°W–82.5°W, 20°S–17.5°S). The error bars are the estimated errors of the mean values obtained using the variance of hourly means. The black curve is the mean diurnal regression fit computed from TMI regression coefficients. Maps of the annual mean (b) amplitude and (c) phase of the LWP diurnal cycle.

The annual mean amplitude and phase of the diurnal cycle over the southeast Pacific Ocean for the year 2014 is shown in Figures 4b and 4c, respectively. The amplitude is calculated from FY-3B/C MWRI data using the regression coefficients in equation (3), that is, $A = \sqrt{A_1^2 + A_2^2}$. The maximum amplitude is located near 85°W/20°S (Figure 4b), and the maximum phase is seen ~0300 LST (Figure 4c). Parallel to the Peruvian coast and ~300 km offshore, the amplitude reaches a maximum of ~0.015 mm at ~0600 LST. Over most areas of the southeast Pacific Ocean, the maximum amplitude of the LWP diurnal cycle appears in the early morning
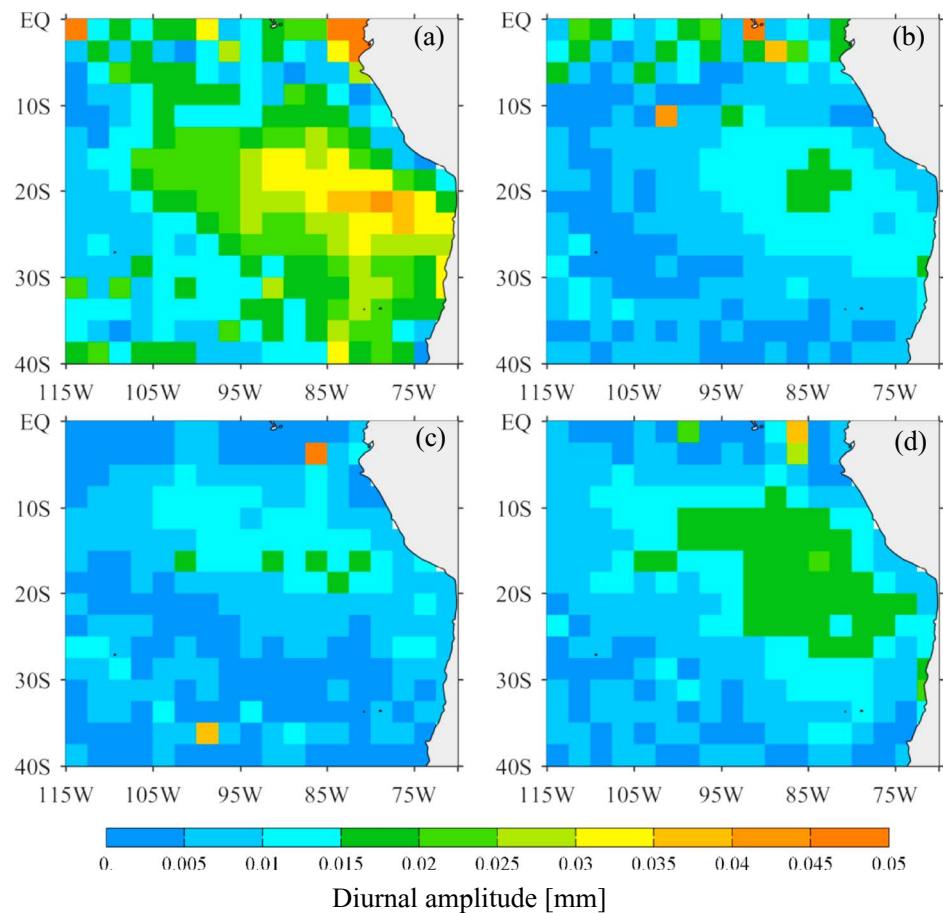
Figure 5. Spatial distribution of the amplitude of the liquid water path diurnal cycle in (a) summer (December-January-February), (b) autumn (March-April-May), (c) winter (June-July-August), and (d) spring (September-October-November) over the Southeast Pacific Ocean. The spatial resolution is 2.5° × 2.5°.

(Figure 4c). The amplitude and phase of the LWP diurnal cycle derived from FY-3B/C MWRIs are consistent with those from previous studies (O'Dell et al., 2008; O'Neill et al., 2011).

3.2. Seasonal Variation of the LWP Diurnal Cycle Amplitude

The seasonal variation of the amplitude of the LWP diurnal cycle is examined here. LWP values for the four seasons are first calculated using FY-3B/C MWRI observations at 0140, 1015, 1340, and 2215 LST in equation (3). The diurnal cycle amplitudes for the different seasons are then derived for the southeast Pacific Ocean. The seasons in the southern hemisphere are defined as summer (December-January-February), autumn (March-April-May), winter (June-July-August), and spring (September-October-November). The diurnal cycle amplitude distributions for each season are shown in Figure 5. The amplitude peaks in austral summer and reaches its minimum in austral winter. Specifically, the amplitude in austral summer varies from 0.02 to 0.04 mm and is strongest near 85°W/20°S. In spring and winter, the amplitudes are relatively small (0.01–0.02 mm). The seasonal variation of the mean LWP amplitude is more than that of the mean LWP by 20%, similar to that in the top-of-the-atmosphere solar flux change over the year (Wood et al., 2002). These results are qualitatively consistent with those from previous studies (O'Dell et al., 2008; O'Neill et al., 2011; Wood et al., 2002; Zuidema & Hartmann, 1995).

4. Conclusions

The diurnal cycle of LWP over the southeast Pacific Ocean is derived from MWRI measurements made from the afternoon FY-3B and midmorning FY-3C satellites. LWP varies temporally and spatially over the southeast

Pacific, reaching its maximum and minimum values in the early morning and afternoon, respectively. The amplitude of the diurnal cycle differs from season to season. The amplitude in winter is larger than in other seasons. The mean amplitude is more than the mean LWP by 20% in most regions. The amplitude reaches 40% of the mean LWP in the region defined by 85°W–82.5°W, 20°S–17.5°S.

Compared to previous studies of LWP over the southeast Pacific Ocean, combined FY-3B/C MWRI data can capture LWP diurnal cycle features reasonably well. However, due to the complexity of clouds over global oceans, a more in-depth examination of the LWP diurnal cycle is needed. This will be addressed in future work.

References

Biswas, S., Gopalan, K., Jones, W., & Bilanow, S. (2010). Correction of time varying radiometric errors in TRMM microwave imager calibrated brightness temperature products. *IEEE Geoscience and Remote Sensing Letters*, 7(4), 851–855. https://doi.org/10.1109/LGRS.2010.2050135

Chen, H., Zou, X., & Qin, Z. (2018). Effects of diurnal adjustment on biases and trends derived from inter-sensor calibrated AMSU-A data. *Frontier of Earth Science*, 12(1), 1–16. https://doi.org/10.1007/s11707-017-0671-y

Duncan, D. I., & Kummerow, C. D. (2016). A 1DVAR retrieval applied to GMI: Algorithm, description, validation, and sensitivities. *Journal of Geophysical Research: Atmospheres*, 121, 7415–7429. https://doi.org/10.1002/2016JD024808

Garreaud, R. D., & Munoz, R. (2004). The diurnal cycle in circulation and cloudiness over the subtropical Southeast Pacific: A modeling study. *Journal of Climate*, 17(8), 1699–1710. https://doi.org/10.1175/1520-0442(2004)017%3C1699:TDCICA%3E2.0.CO;2

Gopalan, K., Jones, W. L., Biswas, S., & Wilheit, T. (2009). A time-varying radiometric bias correction for the TRMM microwave imager. *IEEE Transactions on Geoscience and Remote Sensing*, 47(11), 3722–3730. https://doi.org/10.1109/TGRS.2009.2028882

Gray, W. M., & Jacobson, R. W. (1977). Diurnal variation of deep cumulus convection. *Monthly Weather Review*, 105(9), 1171–1188. https://doi.org/10.1175/1520-0493(1977)105%3C1171:DVODCC%3E2.0.CO;2

Grody, N. C., & Ferraro, R. R. (1992). A comparison of passive microwave rainfall retrieval methods. In *Proceedings of the Sixth Conference on Meteorology and Oceanography* (pp. 60–65). Boston, MA: American Meteorological Society.

Han, Y., Weng, F., Liu, Q., & van Delst, P. (2007). A fast radiative transfer model for SSMIS upper atmosphere sounding channels. *Journal of Geophysical Research*, 112, D11121. https://doi.org/10.1029/2006JD008208

Hargens, U. (1992). Remote sensing of cloud liquid water during ICE'89. Paper presented at the Third Specialist Meeting on Microwave Radiometry and Remote Sensing Applications, Boulder, CO.

Kachi, M., Imaoka, K., Fujii, H., Shibata, A., Kasahara, M., Iida, Y., et al. (2008). Status of GCOM-W1/AMSR2 development and science activities. In R. Meynart, S. P. Neeck, H. Shimoda, & S. Habib (Eds.), *Proceedings of the SPIE on Sensors, Systems, and Next-Generation Satellites XII* (Vol. 7106, pp. 71060P-1–71060P-8). Bellingham, WA: SPIE. https://doi.org/10.1117/12.801228

Kummerow, C., Barnes, W., Kozu, T., Shiue, J., & Simpson, J. (1998). The Tropical Rainfall Measuring Mission (TRMM) sensor package. *Journal of Atmospheric and Oceanic Technology*, 15(3), 809–817. https://doi.org/10.1175/1520-0426(1998)015%3C0809:TTRMMT%3E2.0.CO;2

Kummerow, C., Hong, Y., Olson, W. S., Yang, S., Adler, R. F., McCollum, J., et al. (2001). The evolution of the Goddard Profiling Algorithm (GPROF) for rainfall estimation from passive microwave sensors. *Journal of Applied Meteorology*, 40(11), 1801–1820. https://doi.org/10.1175/1520-0450(2001)040%3C1801:TEOTGP%3E2.0.CO;2

Minnis, P., & Harrison, E. F. (1984). Diurnal variability of regional cloud and clear-sky radiative parameters derived from GOES data. Part I: Analysis method. *Journal of Applied Meteorology*, 23(7), 993–1011. https://doi.org/10.1175/1520-0450(1984)023%3C0993:DVORCA%3E2.0.CO;2

O'Dell, C. W., Wentz, F. J., & Bennartz, R. (2008). Cloud liquid water path from satellite-based passive microwave observations: A new climatology over the global ocean. *Journal of Climate*, 21(8), 1721–1739. https://doi.org/10.1175/2007JCLI1958.1

O'Neill, L. W., Wang, S., & Jiang, Q. (2011). Satellite climatology of cloud liquid water path over the Southeast Pacific between 2002 and 2009. *Atmospheric Chemistry and Physics Discussions*, 11(11), 31,159–31,206. https://doi.org/10.5194/acpd-11-31159-2011

Shupe, M. D., & Intrieri, J. M. (2004). Cloud radiative forcing of the arctic surface: The influence of cloud properties, surface albedo and solar zenith angle. *Journal of Climate*, 17(3), 616–628. https://doi.org/10.1175/1520-0442(2004)017%3C0616:CRFOTA%3E2.0.CO;2

Tang, F., & Zou, X. (2017). Liquid water path retrieval using the lowest frequency channels of Fengyun-3C MicroWave Radiation Imager. *Journal of Meteorological Research*, 31(6), 1109–1122. https://doi.org/10.1007/s13351-017-7012-7

Taylor, K. E., & Ghan, S. J. (1992). An analysis of cloud liquid water feedback and global climate sensitivity in a general circulation model. *Journal of Climate*, 5(9), 907–919. https://doi.org/10.1175/1520-0442(1992)005%3C0907:AAOCLW%3E2.0.CO;2

Weng, F. (2007). Advances in radiative transfer modeling in support of satellite data assimilation. *Journal of the Atmospheric Sciences*, 64(11), 3799–3807. https://doi.org/10.1175/2007JAS2112.1

Weng, F., & Grody, N. C. (1994). Retrieval of cloud liquid water using the Special Sensor Microwave Imager (SSM/I). *Journal of Geophysical Research*, 99(D12), 25,535–25,551. https://doi.org/10.1029/94JD02304

Wood, R., Bretherton, C. S., & Hartmann, D. L. (2002). Diurnal cycle of liquid water path over the subtropical and tropical oceans. *Geophysical Research Letters*, 29(23), 2092. https://doi.org/10.1029/2002GL015371

Yang, S., Weng, F., Yan, B., Sun, N., & Goldberg, M. (2011). Special Sensor Microwave Imager (SSM/I) inter-sensor calibration using a simultaneous conical overpass technique. *Journal of Applied Meteorology and Climatology*, 50(1), 77–95. https://doi.org/10.1175/2010JAMC2271.1

Zuidema, P., & Hartmann, D. L. (1995). Satellite determination of stratus cloud microphysical properties. *Journal of Climate*, 8(6), 1638–1657. https://doi.org/10.1175/1520-0442(1995)008%3C1638:SDOSCM%3E2.0.CO;2